Medium-range ordering, structural heterogeneity, and their influence on properties of Zr-Cu-Co-Al metallic glasses

Soohyun Im, Yuchi Wang, Pengyang Zhao, Geun Hee Yoo, Zhen Chen, Gabriel Calderon, Mehrdad Abbasi Gharacheh, Menglin Zhu, Olivia Licata, Baishakhi Mazumder, David A. Muller, Eun Soo Park, Yunzhi Wang, and Jinwoo Hwang

Phys. Rev. Materials **5**, 115604 — Published 15 November 2021
DOI: 10.1103/PhysRevMaterials.5.115604

Medium Range Ordering, Structural Heterogeneity and Their Influence on Properties of Zr-Cu-Co-Al Metallic Glasses

Soohyun Im[1], Yuchi Wang[1], Pengyang Zhao[1,2], Geun Hee Yoo[3], Zhen Chen[4], Gabriel Calderon[1], Mehrdad Abbasi Gharacheh[1], Menglin Zhu[1], Olivia Licata[5], Baishakhi Mazumder[5], David A. Muller[4,6], Eun Soo Park[3], Yunzhi Wang[1], and Jinwoo Hwang[1, *]

1. Department of Materials Science and Engineering, The Ohio State University, Columbus, OH 43212, USA
2. Department of Engineering Mechanics, Shanghai Jiao Tong University, 800 Dongchuan Road, Shanghai, 200240, China
3. Department of Materials Science and Engineering, Research Institute of Advanced Materials & Institute of Engineering Research, Seoul National University, Seoul 08826, Republic of Korea
4. School of Applied and Engineering Physics, Cornell University, Ithaca, NY 14853, USA
5. Department of Materials Design and Innovation, University at Buffalo-SUNY, Buffalo, NY, USA
6. Kavli Institute at Cornell for Nanoscale Science, Cornell University, Ithaca, NY 14853, USA

* Corresponding author

Abstract

Medium range ordering (MRO) and structural heterogeneity in Zr-Cu-Co-Al metallic glasses (MGs) are characterized and their influence on ductility is investigated. Angular correlation analysis and digital reconstruction of dark-field images of nanodiffraction patterns acquired using four-dimensional scanning transmission electron microscopy reveal structural symmetries of the MRO regions localized at the nanometer scale, as well as their size distribution. The type and size distribution of the MRO regions change as a function of MG composition, with some MRO types clearly resembling the symmetry of known intermetallic phases. The MRO appears to become more structurally frustrated (e.g., lack of 6-fold symmetry) when compositional heterogeneity increases, which may be inherently connected to the observed increase in ductility. Based on this hypothesis, mesoscale deformation simulations incorporating the experimentally acquired MRO information (types and sizes) are performed to gain insights on potential MRO-ductility relationship. Different types of MRO are assumed to have different properties and their influences on the stress-strain curve, the largest connected-free-volume, and the total number of extreme strain value sites are investigated parametrically. The simulation results reveal that the degree of heterogeneity in the MRO structures, both in terms of type and size, correlates directly with the ductility of the MGs.

1. Introduction

Different from crystalline solids where well-defined and well-characterized extended defects such as dislocations and grain boundaries dictate the deformation processes, identifying and understanding the exact deformation mechanisms in amorphous materials are still semantically complex. In metallic glasses (MGs), the deformation has been characterized as "flow" events, which are initiated from nanoscale volumes of the material known as shear transformation zones (STZs) [1,2] that undergo shear deformation under loads. Depending on temperature, STZs can be "activated" either in the entire volume of the material (*i.e.*, homogeneous flow at high temperature) or at localized volumes in the material (*i.e.*, heterogeneous flow at room temperature). For a heterogeneous flow, STZs can concentrate into thin band-like regions known as shear bands, and the localized strain at the shear bands typically lead to brittle failure of the material. Brittle failure of MGs has been the major obstacle for their widespread application albeit their superior properties including exceptionally high strength [3].

Despite the fact that shear banding behavior has been widely observed in MGs, one aspect that has not been understood is why some MGs are significantly more ductile than the others. MGs can display a wide range of ductility: while most MGs are brittle, some MGs have shown dramatic increases in ductility with only a small change in their compositions [4–6]. For example, the Zr-Cu-Co-Al MG used in this study shows a significant increase in ductility at $Zr_{50}Cu_{25}Co_{12.5}Al_{12.5}$ (see Fig. 2b). However, the mechanism of this remarkable effect remains unknown. More specifically, there is no established knowledge on how the atomic structure changes with composition, and how it in turn affects the deformation behavior. Free volumes have been frequently used to explain MG deformation in the past (*e.g.* [2]), but they often show no direct connection to the ductility or other properties [7,8], making it difficult to use the free volume theory alone in general. Theoretical studies have also suggested potential plasticity careers in MGs, such as STZs, or mechanically soft spots in MGs that are closely related to the atomic structures at nanoscale [8–12]. Since the suggested length scale of such plasticity careers is typically at one to a few nanometers, one may hypothesize potential inherent connection between the plasticity career and nanoscale structure of MGs.

Techniques based on atomic force microscopy have shown that some of the MGs' mechanical properties could be linked directly to the nanoscale structure that is heterogeneous in nature (*e.g.* [13–18]), although the detailed connection remains unclear.

The challenge is then to understand the details of such nanoscale structures and their heterogeneous nature (in terms of type, size, volume fraction, spatial distribution, etc.), and how they correlate to properties. Pair distribution function (PDF) [19–21] is typically not sensitive to heterogeneities at the nanometer scale because it shows structural information averaged over the area illuminated by a large probe. Instead, the nanoscale structure has been probed and studied using electron nano-beam diffraction [22] combined with different analysis methods, including fluctuation microscopy that quantifies the variance of diffracted intensities from local volumes as the measure of structural heterogeneity [23–29], and angular correlation analyses of the nanodiffraction patterns that reveal the symmetry of the atomic structures residing in the nanoscale volumes [30,31]. These analyses have revealed that MG structures contain various medium range ordering (MRO) constituting the structural heterogeneity, which represents nanoscale volumes that include relatively high degree of atomic ordering. Previous fluctuation microscopy studies have shown that the type and degree of MRO are correlated with different properties of MGs, including structural relaxation [25], devitrification [28], and potentially shear band formation [29]. Meanwhile, atomistic models have also provided valuable insights into the possible atomic structures at the MRO scale, for instance, potential MRO formation by gathering of nearest neighbor clusters (*e.g.*, icosahedral clusters [32–34]). However, due to the limits of these models, *e.g.*, the extreme quenching rates in molecular dynamics (MD) simulations, it is unclear how the MRO models from these simulations compare to the MRO in real MGs whose cooling history is drastically different from that afforded in MD simulations. For example, the extreme kinetics in these models may not allow the retention of MROs with high structural symmetry (*e.g.*, crystal-like) found in glass forming liquids (*e.g.* [35]) when quenched into glass states. Such MROs with high structural symmetry have been in fact observed in MGs experimentally (*e.g.* [25]), but it is typically missing in molecular dynamics (MD) simulations of MGs [36].

In this work, we tackle the question regarding the structural origin of the substantial change in ductility by small composition variation using a combination of electron nanodiffraction and mesoscale deformation simulation. The goal is to investigate how the MROs of real MGs vary with composition and how such variation potentially impacts the ductility and overall deformation of the MGs. Small composition changes typically do not significantly alter PDF, suggesting that the resulting structural changes may involve heterogeneity at the nanometer scale. We acquire electron nanodiffraction patterns based on 4-dimensional scanning transmission electron microscopy (4D-STEM) [37], followed by angular correlation and direct MRO mapping by reconstruction of the 4D data to acquire statistically reliable information about the MRO and structural heterogeneity in Zr-Cu-Co-Al MGs. Our 4D-STEM method utilizes the electron microscopy pixel array detector (EMPAD) with high dynamic range [37,38] and reveals the local heterogeneity that provides direct MRO information, including the type (symmetry) and size distribution of MRO domains with high statistical precision. We show that the types and sizes of the MRO changes in three different MGs, $Zr_{45}Cu_{50}Al_5$, $Zr_{55}Co_{25}Al_{20}$, and $Zr_{50}Cu_{25}Co_{12.5}Al_{12.5}$. Using angular correlation analysis that reveals the symmetries of the MRO regions, we show that structures of MRO resemble those of stable intermetallic phases in each composition, which appears more prominently than the smaller icosahedral ordering within the structure. Smaller and more structurally frustrated MROs were observed in $Zr_{50}Cu_{25}Co_{12.5}Al_{12.5}$, which may be correlated with the substantially increased ductility in this composition.

Based on the hypothesis that the difference in their MRO structure is inherently connected to the ways STZs are activated, we then use a heterogeneously randomized STZ model to incorporate the experimentally determined MRO type and size to show the correlation between MRO and shear banding behavior. These simulations integrate the characteristics of MRO domains revealed directly in the experiments and study their impact on the overall deformation of MGs beyond the spatial and temporal limits of atomistic simulations [39–41]. Different shear transformation properties of the MRO domains are considered, including numbers of shear modes, activation energy barrier, stress-free transformation strain, and softening behavior. The simulation results reveal that the degree of heterogeneity in the MRO structures, both in terms of type and size, correlates directly with the ductility of the MGs. If the MRO regions are difficult to activate (*i.e.*, difficult to plastically deform) relative to the glassy matrix during deformation, they make the shear bands more diffuse and thus the MGs become more ductile. However, different types of MROs do not exhibit significant difference in such a case. On the other hand, if the MRO domains can be easily activated during plastic deformation, MROs having high symmetry make the glass more brittle while MROs having low symmetry make the MGs more ductile. In both cases, larger MRO size leads to lower ductility.

2. Methods

2.1. Metallic glass sample preparation

The material used in this study is essentially a combination of two MGs, $Zr_{45}Cu_{50}Al_5$ and $Zr_{55}Co_{25}Al_{20}$, with varying relative weights between them [6]. MG ingots with compositions of $(Zr_{45}Cu_{50}Al_5)_{1-x}(Zr_{55}Co_{25}Al_{20})_x$ (x = 0, 0.5, and 1) were prepared by the arc-melting with high purity elements of Zr (99.9 %), Cu (99.9 %), Co (99.9 %) and Al (99.9 %) under Ti-gettered Ar atmosphere. The MGs were flipped and re-melted more than six times within a minute to ensure overall compositional homogeneity. From that, MG ribbons were fabricated by melt-spinning: the alloy melt was put in a quartz tube of an induction heater, which has a circular nozzle with 1.2 mm in diameter and injected over 50 kPa to a rotating copper wheel with a surface velocity of 20 m/s. The as-spun ribbons were 75 ± 5 μm thick and 4.5 ± 0.2 mm wide. We then used the conventional lift-out methods in a focused ion beam (Thermo Fisher Helios) to prepare TEM samples with ion beam energies of 30 keV, followed by 5 keV. For further thinning and cleaning the specimens, we used low energy ion milling (Fischione Nanomill) at 900 eV, followed by 500 eV (5 minutes each).

2.2. Atom probe tomography

Local compositions of each MG samples (x = 0, 0.5, and 1) were analyzed using atom probe tomography (APT). APT samples (needle-shaped tips) were prepared in a Thermo Fisher Nova 200 Focused Ion Beam, using standard milling techniques. APT analysis was performed on the sharpened tips in a LEAP 5000 XR system (CAMECA) under laser-pulse mode with 100 pJ pulse energy, 60 K base temperature, and 0.005 ions/pulse detection.

2.3. 4D-STEM experiment and analysis

4D-STEM was performed to acquire electron nanodiffraction patterns in 2D reciprocal space (k_x, k_y) throughout many MG sample areas (probe positions, p) in 2D real space (x, y) with spatial oversampling of electron probes with a diameter of 1.0 nm [37] (Fig. 1a), using a Cornell/Thermo Fisher EMPAD with a 32-bit dynamic range essential for the quantitative analysis [38] installed in a Thermo Fisher Scientific Titan Themis STEM operated at 300 kV. The 1 nm-sized probe was formed with a 50 μm C_2 aperture and 0.67 mrad convergence half-angle. The probe was scanned using a 1 ms exposure time, and the detector readout time was 0.86 ms. The probe was scanned using 0.16 nm step size and 256 by 256 scanning points at the magnification of 2.4 Mx, covering each sample area of 40 by 40 nm^2. Data were collected from at least 4 sample areas per composition, which gives 262,114 total nanodiffraction patterns for composition. MG TEM specimens usually have thickness gradient because of the way we prepare them in the focused ion beam, and the thicker region of the sample (over ~35 nm thick) can create unwanted artifacts in the data, especially in the angular correlation function due to plural scattering [30,37,42]. On the other hand, if the specimen is too thin (less than ~20 nm), the contribution from the surface oxide layers (usually a few nanometers thick) to the signal may become significant. To avoid these issues, we used the sample area that has the thickness range within ~ 25 to 35 nm. The sample thickness was estimated using the zero-beam electron transmittance method [43].

Angular correlation analysis [42,44] was applied to the 4D nanodiffraction data to determine the structural symmetry of the MRO. The angular correlation, $C(\varphi)$, is the autocorrelation between the pixel intensities in each diffraction pattern as a function of the azimuthal angle, φ (0 to 2π), averaged over the entire θ (0 to 2π), and normalized by the average pixel intensities over the entire θ, for each k (see the notation in Fig. 1b).

$$C(\varphi) = \left[\langle I(\theta) I(\theta + \varphi)\rangle_\theta - \langle I(\theta)\rangle_\theta^2\right] / \langle I(\theta)\rangle_\theta^2 , \tag{1}$$

where I is the pixel intensity, and $\langle I(\theta)\rangle_\theta$ is the pixel intensity averaged over the entire θ. k is the inverse of the real space distance, d, and $C(\varphi)$ was calculated for the entire k range captured in the nanodiffraction pattern. Once $C(\varphi)$ was calculate for each pattern, it was averaged over the entire probed area of the sample to gain statistical significance of the data [31]. Angular correlation analysis has previously been used to determine the icosahedral ordering at the length scale of ~ 0.5 nm [30], but here, we are detecting the structural symmetry of MRO which extends to about one to a few nanometers (which matches with the electron probe size that we used). The diffraction pattern was completely free of any astigmatism to ensure the quality of the angular correlation data.

Average MRO sizes were determined by quantitative analysis of the pixel intensities in the virtual dark-field images reconstructed from the 4D nanodiffraction data. As shown in Fig. 1a, since we know exactly which point (p_1, p_2, p_3, …) of the sample each nanodiffraction pattern was acquired from, the dark-field images of the sample can be digitally reconstructed using the virtual aperture (i_1, i_2, i_3, …) at any (k_x, k_y) pixel, with 40×40 nm^2 in size for the entire φ range (Fig. 1a) and the scattering vector magnitude, k, up to ~ 6 nm^{-1} [37]. The probe positions were overlapped so that we do not miss any points on the sample (top left figure in Fig. 1a). The example dark-field images for k = 4 nm^{-1} with two different φ's are shown in Fig. 1c and 1d. These images show the nanoscale speckles with high intensities, which are the electron intensities scattered by the local MRO toward that particular k and φ. In those MRO regions, k should be related to the type of the MRO since $k = 1/d$, where d is the real space spacing between the diffracting atomic planes (*i.e.* ordering). We then determine the size of MRO speckles within those images for the entire k, by applying a threshold value to each image that reveals the regions of high intensity pixels that must indicate the MRO regions within that area. Unambiguous determination of the threshold value can be challenging because there is no clear boundary between the MRO region and the non-MRO region. Therefore, the threshold values must be determined using a consistent criterion throughout the entire data set. We determined the threshold values based on the intensity histogram from each image. Figure 1e shows an example of histogram (red circles) of the pixel intensities within an image normalized by the average pixel intensity of that image. The histogram has a skewed Gaussian shape, which has an important implication - since one would need a homogeneously random structure to generate a symmetric Gaussian (normal) distribution in the histogram, the fact the histogram shows higher counts to the higher intensity side suggests that there is local heterogeneity in the structure (*i.e.*, MRO) that produces stronger Bragg diffraction. Based on this argument, we fitted a Gaussian function (blue line) to the left side of the histogram (where it assumed to be following the random distribution of the intensity), and the threshold value was determined at the intensity exactly in between the intensities at the Gaussian maximum and the 1% of the Gaussian maximum. An example image with the threshold masking is shown in Fig. 1e inset. While this method provides a statistically consistent way to determine the threshold value, the fact that it ignores the histogram counts that are in between the Gaussian maximum and the threshold value suggests that the method may somewhat underestimate the MRO size. Regardless, since all MRO sizes (from different samples) are expected to systematically change if the threshold method changes, the MRO size comparison (*i.e.*, relative change in MRO size) should not be affected by the potential underestimation. As a comparison, the length scale of the MRO that we detected using this method is also similar to the MRO size measured using the pair persistence analysis of the fluctuation microscopy data from Zr-Cu MGs reported previously [24]. The MRO maps (dark-field images with thresholding, such as shown in Fig. 1e inset) were acquired from all φ angles (126 digitized angles, to be exact) and for all k, per sample area, and the same process was repeated for 4 areas of the sample (and therefore a total of ~262,000 nanodiffraction patterns were used per composition). Using all the MRO maps, 2D histogram of MRO diameter (assuming that MRO regions generally have a spherical shape) vs. k was calculated (Fig. 1f) per composition.

2.4. Mesoscale deformation simulation informed by experiment

A heterogeneously randomized STZ model [39–41] was used to carry out kinetic Monte Carlo (kMC) simulations of plastic deformation of the MGs at nanometer scale. The model contains spatially randomized STZs that are characterized by the number of shear modes, activation energy barrier, transformation strain, and generation-dependent softening behavior, which are different for MRO regions and the glassy matrix. The parameters for MRO regions were determined based on the structural characteristics of MRO measured directly using the 4D-STEM experiment explained above [40]. All the STZ properties are listed in the Table. 1.

3. Results and Discussion

3.1. XRD, compression, DSC, and APT data

The Zr-Cu-Co-Al MGs that we investigated are essentially a mixture of two glass-forming systems [6], $(Zr_{45}Cu_{50}Al_5)_{1-x}$ and $(Zr_{55}Co_{25}Al_{20})_x$. X-ray diffraction (XRD) confirms that all 3 compositions, $Zr_{45}Cu_{50}Al_5$ ($x = 0$), $Zr_{50}Cu_{25}Co_{12.5}Al_{12.5}$ ($x = 0.5$), and $Zr_{55}Co_{25}Al_{20}$ ($x = 1$), have glassy structure without any crystal peaks (Fig. 2a). Stress-strain curve from the compression data shows that, when $x = 0.5$, the glass shows substantial increase in ductility as compared to $x = 0$ and $x = 1$ (Fig. 2b), which is consistent to the previous report by Park et al. [6]. Multiple crystallization peaks at $x = 0.5$ in differential scanning calorimetry (DSC) data (Fig. 2c) have previously led to speculation that there may be phase segregation within the glass [6]. However, the nearest neighbor distribution analyses of the atom probe tomography (APT) data (Fig. 2d) did not detect any chemical segregation, suggesting that if any segregation occurs, it must occur at the scale of a few nanometers or less, which is the length scale typically below the detection level of APT.

3.2. Structural symmetry of MRO from angular correlation analysis

$C(\varphi)$ in Eq. 1 can reveal the rotational symmetry within each nanodiffraction pattern, which can be interpreted as the dominant structural symmetry within the probed volume [42]. It has been shown that, in order to extract statistically meaningful information, $C(\varphi)$ from individual nanodiffraction patterns needs to be averaged over a large volume of the material [31]. Figure 3 shows averaged $C(\varphi)$ calculated from the 4D nanodiffraction data using Eq. (1) for the 3 MG compositions, as a function of k. First, the averaged $C(\varphi)$ of $Zr_{45}Cu_{50}Al_5$ (x = 0, Fig. 4a) shows rich structure, including two hotspots at 180° (indicated with red arrows in Fig. 3a and the corresponding line profile in Fig. 3d), one that has maximum near k ~ 3.96 nm^{-1} and the other near k ~ 4.7 to 5.1 nm^{-1} (maximum at 4.82 nm^{-1}). The two spots indicate that there are multiple types of MRO that show high 2-fold symmetry. There is also a 6-fold symmetry appearing in a broad k range (~ 4 to 5.2 nm^{-1}), as indicated with the white arrows in Fig. 3a and 3d. This MRO with 6-fold symmetry (which is typically a signature of ordered crystals) is consistent to the crystal-like MRO generated by the previous MD simulation including repulsive interaction [35] and the hybrid reverse Monte Carlo simulation including intensity variance data [25]. In addition, 10-fold symmetry appears as weaker shoulder peaks, especially at k ~ 4.8 nm^{-1} (green triangles in Fig. 3d). Ten-fold can be created by the Friedel pairs of 5-fold symmetry, which is the signature of icosahedral clusters that have been predicted to be common in MGs (*e.g.*, [32,33]) and experimentally detected [30,45]. It is therefore likely that the 5-fold signal comes from the glassy structure (non-MRO regions) within the MG where the icosahedral ordering must be present. However, these 10-fold signals are weaker than that of the crystal-like MRO, and this is because the scattering from the smaller (typically ~ 0.5 nm in length) icosahedral ordering must be weaker than that from the bigger (~ 1 to 1.3 nm, see Section 3.3. for details) and more highly ordered crystal-like MRO.

The appearance of 2- and 6-fold ordering suggests that the structure may contain MRO that resembles the structure of the crystalline (intermetallic) phases with similar composition. Based on this assumption, the k peak positions of the spots in Fig. 3a were compared to those of intermetallic phases to gain insights about the MRO structure (indicated at the top of the graph). For instance, the peak position at

$k \sim 3.96\ \mathrm{nm}^{-1}$ is close to the maximum diffraction peaks of 3 different intermetallic phases, Zr_3Al (which has the maximum diffraction peak at $k = 3.95\ \mathrm{nm}^{-1}$ [46–49]), α-Zr (maximum peak at $k = 4.06\ \mathrm{nm}^{-1}$ [50,51]), and $CuZr_2$ (maximum peak at $k = 4.09\ \mathrm{nm}^{-1}$) [52,53], suggesting that the MRO structure may resemble the structure of those phases. Similarly, the broad 2-fold peak at $k \sim 4.87\ \mathrm{nm}^{-1}$ is close to the maximum diffraction peaks of FCC Cu ($k = 4.8\ \mathrm{nm}^{-1}$) and Cu_4Al ($k = 5\ \mathrm{nm}^{-1}$) [54]. In the same way, the k range of ~ 4.2 to 5.2 nm^{-1} where 6-fold is apparent includes the peak positions of CuZr ($\mathrm{Pm}\bar{3}\mathrm{m}$, $k = 4.32\ \mathrm{nm}^{-1}$) Cu_2ZrAl ($\mathrm{Pm}\bar{3}\mathrm{m}$, at $k = 4.55\ \mathrm{nm}^{-1}$) [55–57], as well as FCC Cu ($\mathrm{Fm}\bar{3}\mathrm{m}$, at $k = 4.8\ \mathrm{nm}^{-1}$), all of which have 6-fold symmetry (including 3-folds, which appears as 6-folds due to Friedel symmetry). While these matching peak positions give some insights regarding how MRO structure resembles that of intermetallic phases with similar compositions, we should note that the MRO is not the same as nanocrystals, since the MRO structure is still substantially more disordered (or frustrated) and typically smaller in size as compared to that of previously observed nanocrystalline phases (*e.g.*, [58]).

Same analysis was performed on $Zr_{55}Co_{25}Al_{20}$ (x=1) shown in Fig. 3c. The data shows the highest 2-fold spot at $k \sim 3.95\ \mathrm{nm}^{-1}$ (red arrows in Fig. 3c and 3f), which likely corresponds to MRO resembling Zr_3Al and α-Zr. There is another 2-fold spot that peaks at $k \sim 5\mathrm{nm}^{-1}$, which is close to the major peak position of AlCo ($Pm\bar{3}m$, $k = 4.96\ \mathrm{nm}^{-1}$), $CoZr_2$ ($I4/mcm$, $k = 4.75\ \mathrm{nm}^{-1}$), and Co ($P6_3/\mathrm{mmc}$, $k = 5.22\ \mathrm{nm}^{-1}$). As compared to $Zr_{45}Cu_{50}Al_5$, however, $Zr_{55}Co_{25}Al_{20}$ shows weaker higher-order symmetries: for example, the line profile at $k = 3.85\ \mathrm{nm}^{-1}$ (blue line in Fig. 3f) shows some small peaks but their amplitudes are low and do not exactly correspond to the positions of 4, 5, or 6-fold symmetries, which suggests that the MRO structure is more disordered than those in $Zr_{45}Cu_{50}Al_5$ shown in Fig. 3d. Instead, the amplitude of 2-fold appears to be relatively stronger in this composition, suggesting that 2-fold MRO is more dominant as compared to the MROs with other symmetries.

Lastly, the mixture of two glass-forming compositions, $Zr_{50}Cu_{25}Co_{12.5}Al_{12.5}$, shows dominating two hotspots, one peaks at $k \sim 4\ \mathrm{nm}^{-1}$ and the other at $k \sim 5.1\ \mathrm{nm}^{-1}$ (red arrows in Fig. 3b and 3e). However, signals for the higher order symmetries appear to be lower than the other two compositions (Fig. 3e). This implies that higher order symmetries (*e.g.* 6-folds) are much weaker in this composition, which also appears to have consolidated the low-order symmetry (2-folds) when the two compositions ($Zr_{45}Cu_{50}Al_5$ and $Zr_{55}Co_{25}Al_{20}$) are mixed in $Zr_{50}Cu_{25}Co_{12.5}Al_{12.5}$. For example, the MRO resembling the intermetallic compounds consisting of Zr , Cu, and/or Al atoms may become more frustrated as Co is mixed in, since there is a strong negative bonding enthalpy between Zr and Co [6]. This frustration of MRO observed in angular correlation data also coincides with the smaller MRO size measured in this composition, which will be explained in detail in Section 3.3.

3.3. Direct quantification of MRO sizes from 4D-STEM data

We determined MRO size data as a function of k directly from the virtual dark-field images from 4D nanodiffraction data (Fig. 4), which we also compare to the angular correlation results that we explained above. First, $Zr_{45}Cu_{50}Al_5$ ($x = 0$, red curve in Fig. 4) shows a larger MRO size, with maximum size of ~1.27 nm at $k \sim 4.2$ nm^{-1} which approximately matches the k peak position of the MRO that we attributed to multiple intermetallic phases in the corresponding angular correlation data (Fig. 3a and 3d), especially the ones with high 6-fold ordering. This indicates that, when MRO has high degree of ordering represented by 6-fold symmetry, the MRO may be more stable and therefore its size can be relatively bigger as well. There is also a peak at $k \sim 5$ nm^{-1} (Fig. 4) indicating MRO containing smaller interatomic distances, likely corresponding to MRO made of mostly smaller atoms (*i.e.*, Cu), with its size of ~ 1 nm. This peak position matches that of Cu and Cu_4Al intermetallic phases that we indicated in the angular correlation data in Fig. 3a.

Meanwhile, the $Zr_{55}Co_{25}Al_{20}$ ($x = 1$, blue curve in Fig. 4) shows two peaks, one at k ~3.9 nm^{-1} and the other at ~ 4.9 nm^{-1}, which match the 2-fold peak positions appeared in the corresponding angular correlation data (Fig. 3c and 3f). The smaller MRO size of ~ 1.2 nm at the peak (k ~3.9 nm^{-1}) in this composition as compared to that of $Zr_{45}Cu_{50}Al_5$ at its peak can be correlated to the fact that this composition has less degree of higher order symmetry (*e.g.* 6-folds) as compared to $Zr_{45}Cu_{50}Al_5$, as shown in Fig. 3c and 3f. The peak at $k \sim 5.0$ nm^{-1} in Fig. 4 showing the averaged MRO size of ~ 1 nm can be correlated to Co-rich MROs, such as Co, AlCo, and $CoZr_2$, as indicated in Fig. 3c.

Lastly, the “mixed” composition at $x = 0.5$, $Zr_{50}Cu_{25}Co_{12.5}Al_{12.5}$ (green curve in Fig. 4), shows consistently smaller MRO sizes throughout the wider k range of ~ 3.7 to 4.6 nm^{-1}, as compared to the other two compositions. In addition, the fact that this composition does not show the peaks at k ~3.9 and 4.2 nm^{-1} that are in the red ($Zr_{45}Cu_{50}Al_5$) and blue ($Zr_{55}Co_{25}Al_{20}$) plots, respectively, may suggest that this composition, $Zr_{50}Cu_{25}Co_{12.5}Al_{12.5}$, has more diverse distribution of MRO types without having one MRO size dominating the other. The smaller size and more diverse distribution of MRO types in this composition also connects well with the more disordered (or frustrated) MRO structure that we explained in Fig. 3b and 3e.

In summary of the experimental data, angular correlation analysis and MRO mapping from 4D nanodiffraction data showed that the structural symmetry and the size of MRO are distinctively different in these three compositions, with some MGs having MRO structures resembling that of intermetallic phases. Most importantly, the fact that $Zr_{50}Cu_{25}Co_{12.5}Al_{12.5}$ has more frustrated and smaller MRO than the other two compositions may connect with the fact that this composition showed notably higher ductility than the other two (Fig. 2b). Similar change in plasticity by minor alloying was also recently observed in Pd-based MGs [59]. While the apparent connection we observed experimentally may provide important implication on the composition-MRO-ductility relationship, the mechanism of such potential correlation cannot be verified using our experimental data. Therefore, we incorporated the experimentally determined MRO information to mesoscale deformation simulation to gain insights on this potential correlation, which is explained in the next section.

3.4. Mesoscale deformation simulation incorporating experimetnally determined MRO

To offer some mechanistic insight into the potential correlations between the experimentally obsered MRO structures and experimentally measured ductilities in the three MGs shown in Figs. 3 and 4, we carry out a parametric study of shear banding at nanocale using kinetic Monte Carlo simulations based on a heterogeneously randomized STZ model [40-42]. The simulations incorporate MRO microstructures determined by the 4D-STEM and map different types of MRO directly onto different types of STZs having different numbers of shear modes, activation energy barriers, and softening behavior from the glassy matrix as well as from each other. Such mesoscale simulations go beyond the spatial and temporal limits of MD simulations and allow the consideration of the full development of multiple shear bands [39–41].

Our recent simulations capturing several key MRO features revealed by the fluctuation microscopy [40] showed that the volume fraction and type of MRO (*e.g*., 2-fold vs. 6-fold MRO) have significant impact on shear banding and stress-strain behavior. A new concept, "strain frustration", was proposed, which is essentially related to the geometrical incompatibility caused by dissimilar plastic carriers (*e.g*., different MROs) that exhibit strong bias in favor of certain local slip modes that are different from those of the glassy matrix. Since the local slip modes are greatly influenced by atomic packing, a correlation between the MRO structure and the shear catalog of STZs should be expected naturally. In particular, we hypothesize that (*i*) the number of STZ shear modes is corresponding to the degree of ordering (symmetry, e.g., 2-fold vs. 6-fold) in the corresponding MRO, while it is much smaller than the number of shear modes of glassy matrix with disordered structure, and (*ii*) the degree of softening induced by STZ activation is inversely proportional to the degree of ordering in the corresponding MRO as long as the MRO domains can maintain their ordered structure. The first rule is based on that more ordering leads to more significant bias in favor of certain slip systems, and the MRO symmetry determines the number of biased shear directions; the second rule reflects that a more ordered atomic structure tends to preserve the original lattice sites (with crystals being the extreme case where the lattice is completely preserved after the passage of a full dislocation) and hence leads to less softening (according to the free-volume or extended-defect based damage theory [39,60]).

These rules allow us to parameterize the STZs in different structural components (regions of different types of MROs and glassy matrix) of the MGs. For example, according to the symmetry analysis of the MRO structures from the results shown in Figs. 3 and 4, we consider two extreme cases where dissimilar STZs derived from dissimilar MROs are assumed to have different shear modes, *i.e.*, 6 shear modes in $Zr_{45}Cu_{50}Al_5$ (x = 0) where the angular correlation shows the strongest 6-fold symmetry (Fig. 3a), and 2 shear modes in $Zr_{50}Cu_{25}Co_{12.5}Al_{12.5}$ (x = 0.5) where 6-fold symmetry is weak but 2-fold is strong. Both cases have fewer shear modes as compared to the 20 shear modes of STZs derived from the glassy matrix that is the most disordered structural components in the glasses. The current values assigned to the number of shear modes of STZs can reasonably differentiate the STZ characteristics in different regions, which is essential to test our hypothesis. Besides the number of shear modes, we also assumed different stress-free transformation strains (SFTS) for STZs in different regions (i.e., 2-fold and 6-fold MRO regions and glassy matrix). The SFTS enters the work term in the activation energy barrier calculation, with larger SFTS leading to lower activation energy barrier [42]. The ratio between the SFTS of the MRO and glassy matrix regions is assumed to be 1 for “hard” MROs that are difficult to activate as compared to the glassy matrix, and 2 for “soft” MROs that are easy to activate.

Tensile test simulations of MGs having 6-fold and 2-fold MRO nanodomains were performed with a fixed volume fraction of the MRO regions, all being 10%. For hard MROs, the stress-strain curves and the peak stress appear the same for MGs having either 6-fold or 2-fold MRO domains, but for soft MROs, the MG having 6-fold MRO domains has a lower peak stress and a larger stress-drop in comparing with the MG having 2-fold MRO domains, as shown in Fig. 5a. Note that no damage (failure) model is included yet in the simulations, so the deformation continues. These results indicate that the mechanical behaviors of MGs with dissimilar STZs of different shear modes exhibit a much more pronounced difference when the MRO regions are soft (*i.e.*, the STZs in the MRO regions are easily activated), and the MG having 2-fold MRO domains is more ductile as compared to the MG having 6-fold MRO domains (see more analysis about the deformation microstructure, largest connected-free-volume and extreme value statistics below), which matches well with the experimental results as shown in Fig. 3b. Also, comparing the stress-strain curves for MGs having hard and soft MRO domains, the latter is more brittle. Fig. 5b (left panel) shows the deformation microstructures (*i.e.*, von Mises strain maps) at 2.7% overall elongation for all four stress-strain curves. When the MRO domains are soft, the shear bands are more localized, which makes the MG more brittle. Furthermore, the shear band becomes much sharper and "hotter" (higher locally accumulated plastic strain) in the MG having 6-fold soft MRO domains than the MG having 2-fold soft MRO domains.

The analysis on the largest connected-free-volume (CFV) [39] also shows the difference in these cases. Fig. 5b (right panel) shows the deformation microstructures (*i.e.*, von Mises strain maps) at 3% overall elongation, with the largest CFV superimposed on top of them. It shows that a shear band with the largest CFV goes through the entire sample that has 6-fold soft MRO domains, while it goes through only half of the sample that has 2-fold soft MRO domains. In the case of hard MRO domains, the largest CFVs are still localized in the samples. Since the largest CFV is the most probable location for crack initiation, these results imply that MGs having hard MRO regions may provide the most improved ductility. For MGs having soft MRO domains, the lower the symmetry of the MRO, the higher the ductility, which is consistent with the experimental result in Fig. 3b.

To further analyze the effect of dissimilar STZs in different MGs on their deformation microstructure and damage-tolerance, extreme value (EV) statistics [41] is obtained. In this study, voxels with accumulated transformation strain larger than 0.3 are deemed extreme sites. MGs with less extreme sites can be regarded as more damage-tolerant and more ductile. Fig. 5c shows the average numbers of the extreme sites in the whole system and in the MRO domains obtained for MGs having 6-fold and 2-fold hard and soft MRO domains. To capture the variation in the calculation results due to the randomness, calculations for each case presented in Fig. 5c were repeated 10 times with different random number seeds for spatial distributions of MRO domains, shear directions of each shear mode, random variable in kMC algorithm, and random disturbance of transformation strain, with the error bars being the standard deviations. If the MRO regions are hard (*i.e.*, difficult to be activated or non-sharable), nearly no extreme sites appear within the MRO regions. In this case, different numbers of the available shear modes within the MRO regions would not play a significant rule and the total number of extreme sites are similar in MGs having 6-fold and 2-fold MRO domains. If the MRO regions are soft, much more extreme sites appear within the MRO regions. In this case, the "strain frustration" effect [41] (i.e., the shear modes in the MRO regions are statistically incompatible with those in the glassy matrix because of the mismatch in their shear catalogs), even though weaker as compared to the hard MRO regions, is different in the 6-fold and 2-fold MRO domains. Since the former have more shear modes, they are more compatible in shear deformation with a growing shear band (having more shear modes to choose and, thus, easier to find a mode that has a close shear direction with that of a given shear band). Therefore, the 6-fold MRO regions are easier to be activated and have more extreme sites in comparing with the 2-fold MRO regions. These differences are also reflected well in the stress-strain curves shown in Fig. 5a.

To consider the effect of MRO domain size, we first created additional two MRO maps, with significantly larger mean domain sizes than that observed in the experiment. The overall MRO volume fraction is kept the same. Fig. 5d shows the numbers of extreme sites at 2.7% overall elongation for different cases. It shows that as the MRO domain size increases, the number of the extreme sites in the system also increase, suggesting a more brittle glass. This result is understandable as increasing the MRO domain size while keeping the volume fraction unchanged increases inter-MRO domain spacing and shear bands can easily find MRO-free paths. This argument also applies to the current experimental observations where the volume fractions of the MRO regions in the three samples are not significantly dissimilar (especially for those of $x = 0$ and $x = 0.5$).

Note that only limited cases were considered in this parametric simulation study. For the hard and soft MRO regions, we assume that the transformation strains and the activation energy barriers are the same for both 6-fold and 2-fold, and only the number of shear modes difference is considered. Since the 6-fold MRO structure is more ordered than the 2-fold MRO structure, its activation energy barrier could be higher, while the transformation shear strain could also be higher. Thus, in this case, the activation energy barrier (with the contribution from the work term) can be different. To examine parametrically the effect of different activation energy barriers in different MRO regions, we assume an FCC-like structure in the 6-

fold MRO domains. Based on this assumption, we set a group of new parameters: $\Delta F_* = 2.4\ eV$ and $\gamma = 0.18$. For the 2-fold MRO, we assume the same activation energy barrier as what we have used in our previous simulations, i.e., $\Delta F_* = 2\ eV$, which is smaller than that of the 6-fold MRO. In addition, we considered three new shear strain values for the 2-fold MRO regions for this parametric study, i.e., γ = 0.14, 0.16 and 0.18, all of which are below that of the 6-fold MRO, and also compared the results with the previous simulation results with γ = 0.1 and 0.2. The simulation results are shown in the Fig. 5e. It shows that when the shear strain for the 2-fold MRO regions is smaller than that of the 6-fold, the numbers of extreme sites is smaller in the 2-fold MRO regions. These results may somehow explain the experimental results in another way.

On the other hand, we assumed that the MRO regions do not soften during continued activation of the shear events in the current simulations. However, since the MRO size is very small, the current shearing event may destroy the ordered structure of MROs, leading to significant softening for the subsequent searing events. Therefore, the MRO regions that have been activated will be easier to accumulate more strain. We have also tested parametrically two different softening behaviors for the 6-fold MRO regions. Softening 1 is the same as the glassy matrix, while Softening 2 is twice as much as Softening 1. As can be seen in Fig. 5e, a more severe softening leads to more extreme sites in the MRO regions as long as some sites in the MRO regions can be activated. This softening effect further increases the difference in deformation behavior between samples having 6-fold and 2-fold MRO regions. However, the actual softening behavior for the MRO regions is still unknow and one may have to rely on atomistic simulations [61,62] to obtain critical information on MRO properties.

4. Conclusions

In summary, the 4D-STEM analysis directly determines different MRO structure with various sizes, types and degree of ordering in Zr-Cu-Co-Al MGs and clearly demonstrates the correlation between the ductility of MRO. The result from angular correlation analysis shows that some MRO regions have their structure resembling that of intermetallic phases with similar compositions. In particular, the smaller and more disordered MRO structure correlates with a substantial increase in ductility when two compositions, Zr-Cu-Al and Zr-Co-Al, are mixed into each other. Mesoscale simulation based on the experimentally determined MRO information confirms that the diverse types and sizes of MRO domains can significantly influence the MGs' mechanical behavior. The new information we found is critical as it provides important quantitative details of the structural heterogeneity in MGs and how it connects to their properties, which may serve as an important foundation for establishing new paradigm in designing new amorphous materials with desired structural properties.

Acknowledgement

S.I., P.Z, Y. W and J. H. acknowledge support by the NSF under DMR-1709290, and the partial support by DMR-2104724. This work was performed in part in the Center for Electron Microscopy and Analysis at the Ohio State University, as well as at the Cornell PARADIM Electron Microcopy Facility, as part of the Materials for Innovation Platform Program, which is supported by the NSF under DMR-1539918 with additional infrastructure support from DMR-1719875 and DMR-1429155. D. M. and Z. C. are also supported by PARADIM. G.Y. and E.P were supported by Samsung Research Funding Center of Samsung Electronics under Project Number SRFC-MA1802-06.

Data Availability

The raw data required to reproduce these findings are available to download from the PI's group database at https://hwang.engineering.osu.edu/microscopy-database. The processed data required to reproduce these findings are available to download from the PI's group data base at https://hwang.engineering.osu.edu/microscopy-database.

[1] M. L. Falk, J. S. Langer, and L. Pechenik, Phys. Rev. E **70**, 11507 (2004).

[2] A. S. Argon, Acta Metall. **27**, 47 (1979).

[3] T. C. Hufnagel, C. A. Schuh, and M. L. Falk, Acta Mater. **109**, 375 (2016).

[4] Y. H. Liu, G. Wang, R. J. Wang, D. Q. Zhao, M. X. Pan, and W. H. Wang, Science (80-.). **315**, 1385 LP (2007).

[5] B. Zhang, D. Q. Zhao, M. X. Pan, W. H. Wang, and A. L. Greer, Phys. Rev. Lett. **94**, 205502 (2005).

[6] J. M. Park, J. H. Han, N. Mattern, D. H. Kim, and J. Eckert, Metall. Mater. Trans. A **43**, 2598 (2012).

[7] A. Widmer-Cooper and P. Harrowell, J. Non. Cryst. Solids **352**, 5098 (2006).

[8] M. L. Manning and A. J. Liu, Phys. Rev. Lett. **107**, 108302 (2011).

[9] A. Widmer-Cooper, H. Perry, P. Harrowell, and D. R. Reichman, Nat Phys **4**, 711 (2008).

[10] C. E. Maloney and A. Lemaître, Phys. Rev. E **74**, 16118 (2006).

[11] J. Ding, S. Patinet, M. L. Falk, Y. Cheng, and E. Ma, Proc. Natl. Acad. Sci. **111**, 14052 (2014).

[12] J. Ding, Y.-Q. Cheng, H. Sheng, M. Asta, R. O. Ritchie, and E. Ma, Nat. Commun. **7**, 13733 (2016).

[13] F. Zhu, S. Song, K. M. Reddy, A. Hirata, and M. Chen, Nat. Commun. **9**, 3965 (2018).

[14] D. P. Wang, J. C. Qiao, and C. T. Liu, Mater. Res. Lett. **7**, 305 (2019).

[15] H. B. Ke, J. F. Zeng, C. T. Liu, and Y. Yang, J. Mater. Sci. Technol. **30**, 560 (2014).

[16] H. Ke, C. Liu, and Y. Yang, Sci. China Technol. Sci. **58**, 47 (2015).

[17] M. Gao and J. H. Perepezko, Nano Lett. (2020).

[18] Y. H. Liu, D. Wang, K. Nakajima, W. Zhang, A. Hirata, T. Nishi, A. Inoue, and M. W.

Chen, Phys. Rev. Lett. **106**, 125504 (2011).

[19] E. Takeshi and S. J. L. Billinge, in *Underneath the Bragg Peaks,* edited by T. Egami and S. J. L. B. T.-P. M. S. Billinge (Pergamon, 2012), pp. 55–111.

[20] C. E. Pueblo, M. Sun, and K. F. Kelton, Nat. Mater. **16**, 792 (2017).

[21] D. Ma, A. D. Stoica, and X.-L. Wang, Nat. Mater. **8**, 30 (2009).

[22] J. M. Rodenburg, Ultramicroscopy **25**, 329 (1988).

[23] M. M. J. Treacy, J. M. Gibson, L. Fan, D. J. Paterson, and I. McNulty, Reports Prog. Phys. **68**, 2899 (2005).

[24] J. Hwang and P. M. Voyles, Microsc. Microanal. **17**, 67 (2011).

[25] J. Hwang, Z. H. Melgarejo, Y. E. Kalay, I. Kalay, M. J. Kramer, D. S. Stone, and P. M. Voyles, Phys. Rev. Lett. **108**, 195505 (2012).

[26] P. M. Voyles and D. A. Muller, Ultramicroscopy **93**, 147 (2002).

[27] J. Hwang, A. M. Clausen, H. Cao, and P. M. Voyles, J. Mater. Res. **24**, 3121 (2009).

[28] Y. E. Kalay, I. Kalay, J. Hwang, P. M. Voyles, and M. J. Kramer, Acta Mater. **60**, (2012).

[29] V. Schmidt, H. Rösner, M. Peterlechner, G. Wilde, and P. M. Voyles, Phys. Rev. Lett. **115**, 35501 (2015).

[30] A. C. Y. Liu, M. J. Neish, G. Stokol, G. A. Buckley, L. A. Smillie, M. D. de Jonge, R. T. Ott, M. J. Kramer, and L. Bourgeois, Phys. Rev. Lett. **110**, 205505 (2013).

[31] T. Sun, M. M. J. Treacy, T. Li, N. J. Zaluzec, and J. Murray Gibson, Microsc. Microanal. **20**, 627 (2014).

[32] H. W. Sheng, W. K. Luo, F. M. Alamgir, J. M. Bai, and E. Ma, Nature **439**, 419 (2006).

[33] Y. Q. Cheng, E. Ma, and H. W. Sheng, Phys. Rev. Lett. **102**, 245501 (2009).

[34] D. B. Miracle, Nat. Mater. **3**, 697 (2004).

[35] H. Tanaka, T. Kawasaki, H. Shintani, and K. Watanabe, Nat. Mater. **9**, 324 (2010).

[36] J. Wen, Y. Q. Cheng, J. Q. Wang, and E. Ma, J. Appl. Phys. **105**, 43519 (2009).

[37] S. Im, Z. Chen, J. M. Johnson, P. Zhao, G. H. Yoo, E. S. Park, Y. Wang, D. A. Muller, and J. Hwang, Ultramicroscopy **198**, 189 (2018).

[38] M. W. Tate, P. Purohit, D. Chamberlain, K. X. Nguyen, R. Hovden, C. S. Chang, P. Deb, E. Turgut, J. T. Heron, D. G. Schlom, D. C. Ralph, G. D. Fuchs, K. S. Shanks, H. T. Philipp, D. A. Muller, and S. M. Gruner, Microsc. Microanal. **22**, 237 (2016).

[39] P. Zhao, J. Li, and Y. Wang, Acta Mater. **73**, 149 (2014).

[40] P. Zhao, J. Li, J. Hwang, and Y. Wang, Acta Mater. **134**, 104 (2017).

[41] P. Zhao, J. Li, and Y. Wang, Int. J. Plast. **40**, 1 (2013).

[42] P. Wochner, C. Gutt, T. Autenrieth, T. Demmer, V. Bugaev, A. D. Ortiz, A. Duri, F. Zontone, G. Grübel, and H. Dosch, Proc. Natl. Acad. Sci. **106**, 11511 (2009).

[43] D. T. Schweiss, J. Hwang, and P. M. Voyles, Ultramicroscopy **124**, (2013).

[44] S. Im, Z. Chen, J. M. Johnson, P. Zhao, G. H. Yoo, E. S. Park, Y. Wang, D. A. Muller, and J. Hwang, Ultramicroscopy **195**, 189 (2018).

[45] A. Hirata, P. Guan, T. Fujita, Y. Hirotsu, A. Inoue, A. R. Yavari, T. Sakurai, and M. Chen, Nat. Mater. **10**, 28 (2010).

[46] C. Li, J. She, M. Pang, W. Yang, and Y. Zhan, J. Phase Equilibria Diffus. **32**, 24 (2011).

[47] W. J. Meng, J. jr. Faber, P. R. Okamoto, L. E. Rehn, B. J. Kestel, and R. L. Hitterman, J. Appl. Phys. **67**, 1312 (1990).

[48] J. H. Keeler and J. H. Mallery, J. Met. **7**, 394 (1955).

[49] Y. H. Duan, B. Huang, Y. Sun, M. J. Peng, and S. G. Zhou, J. Alloys Compd. **590**, 50 (2014).

[50] L. E. Tanner and R. Ray, Acta Metall. **27**, 1727 (1979).

[51] K. Lejaeghere, V. Van Speybroeck, G. Van Oost, and S. Cottenier, Crit. Rev. Solid State Mater. Sci. **39**, 1 (2014).

[52] M. V Nevitt and J. W. Downey, Trans. Metall. Soc. Aime **224**, 195 (1962).

[53] T. A. Sviridova, N. P. Diakonova, E. V Shelekhov, and V. P. Glazkov, Poverkhnostnye Fiz. Khimiya, Mekhanika **2004**, 28 (2004).

[54] J. L. Leach, J INST MET **92**, 93 (1964).

[55] W. Heine and U. Zwicker, Naturwissenschaften **49**, 5 (1962).

[56] G. S. Firstov, Y. N. Koval', A. N. Timoshevskii, and J. Van Humbeeck, Dopov. Nats. Akad. Nauk. Ukr. **2010**, 103 (2010).

[57] C. S. Xin, X. X. Guang, H. H. Quan, L. Z. Tao, Z. G. Qing, and G. Z. Zheng, Phys. B, Condens. Matter **406**, 3389 (2011).

[58] R. J. H. E.-Y. Masuda, in (IntechOpen, Rijeka, 2011), p. Ch. 4.

[59] S. Hilke, H. Rösner, and G. Wilde, Scr. Mater. **188**, 50 (2020).

[60] L. Li, E. R. Homer, and C. A. Schuh, Acta Mater. **61**, 3347 (2013).

[61] Y. Fan, T. Iwashita, and T. Egami, Nat. Commun. **5**, 5083 (2014).

[62] Y. Fan, T. Iwashita, and T. Egami, Nat. Commun. **8**, 15417 (2017).

Table and Figure Captions

Table 1. List of simulation parameters

Figure 1. (a) Schematic of 4D-STEM. Nanodiffraction patterns are acquired using electron probe (diameter = 1 nm) from oversampled probe positions (p_1, p_2, ..) on the sample. The intensities (i_1, i_2 ,..) in the acquired stack of patterns are reconstructed in the real space by selecting any (k_x, k_y) pixel within the pattern. (b) An example nanodiffraction pattern. (c and d) The reconstructed dark-field images using the "$I(\theta)$" and "$I(\theta + \varphi)$" locations in (b), respectively. (e) An example histogram of the normalized pixel intensities within a reconstructed image (red circles), a Gaussian fit to the left side of the histogram (blue line), and the location of the threshold value. The inset shows a dark field image from $Zr_{45}Cu_{50}Al_5$ (x = 0) after the threshold mask is applied. Red areas indicate the areas with high intensity above the threshold. (f) 2-D histograms of the average MRO diameter (in nm) as a function of k, calculated from the dark field images.

Figure 2. Experimental (a) X-ray diffraction, (b) compression, (c) DSC, and (d) atom probe tomography data from $(Zr_{45}Cu_{50}Al_5)_{1-x}(Zr_{55}Co_{25}Al_{20})_x$ (x = 0, 0.5, and 1).

Figure 3. Maps of averaged angular correlation, $C(\varphi)$, as a function of k, from (a) $Zr_{45}Cu_{50}Al_5$ (x = 0), (b) $Zr_{50}Cu_{25}Co_{12.5}Al_{12.5}$ (x = 0.5), and (c) $Zr_{55}Co_{25}Al_{20}$ (x = 1). (d, e, and f) The line profiles for different k values indicated with the white dashed lines on (a), (b), and (c), respectively. In (d), the profiles are shifted vertically for visual clarity.

Figure 4. Average MRO size vs. k from $Zr_{45}Cu_{50}Al_5$ (x = 0), $Zr_{50}Cu_{25}Co_{12.5}Al_{12.5}$ (x = 0.5), and $Zr_{55}Co_{25}Al_{20}$ (x = 1). Color shadows indicate standard deviation of mean.

Figure 5. (a) Simulated stress-strain curves for $(Zr_{45}Cu_{50}Al_5)_{1-x}(Zr_{55}Co_{25}Al_{20})_x$ (6-fold for x = 0 and 2-fold for x = 0.5) with hard and soft MROs. (b) The deformation microstructures (Von Mises strain maps) at 2.7% overall elongation for all four curves in (a) at left two columns, and the Von Mises strain maps (red dots) at 3% overall elongation and superposition of the largest connected-free-volume (cyan dots) on top of them. (c) Average numbers of extreme sites of the whole system and within the MROs, together with the error representing the standard deviation. (d) Average numbers of extreme sites with different MRO sizes, with the error being the standard deviation. (e) Average numbers of extreme sites with different shear strain for 2-fold MRO regions without softening, and the average numbers of extreme sites for 6-fold MRO regions with different softening behaviors as references (dash lines).

Parameter	Value
Young's modulus E	69.46 GPa [40]
Poisson's ratio ν	0.365 [40]
Helmholtz free energy difference ΔF_*	2.5 eV (for the glassy matrix)
	2 eV (for the MRO)
Shear strain γ	0.1 (for the glassy matrix)
	0.1 (for the hard MRO)
	0.2 (for the soft MRO)
Number of shear modes M	20 (for the glassy matrix)
	6 (for the 6-fold MRO)
	2 (for the 2-fold MRO)
Softening behavior	Yes (for the glassy matrix)
	No (for the MRO)

Table 1. List of simulation parameters

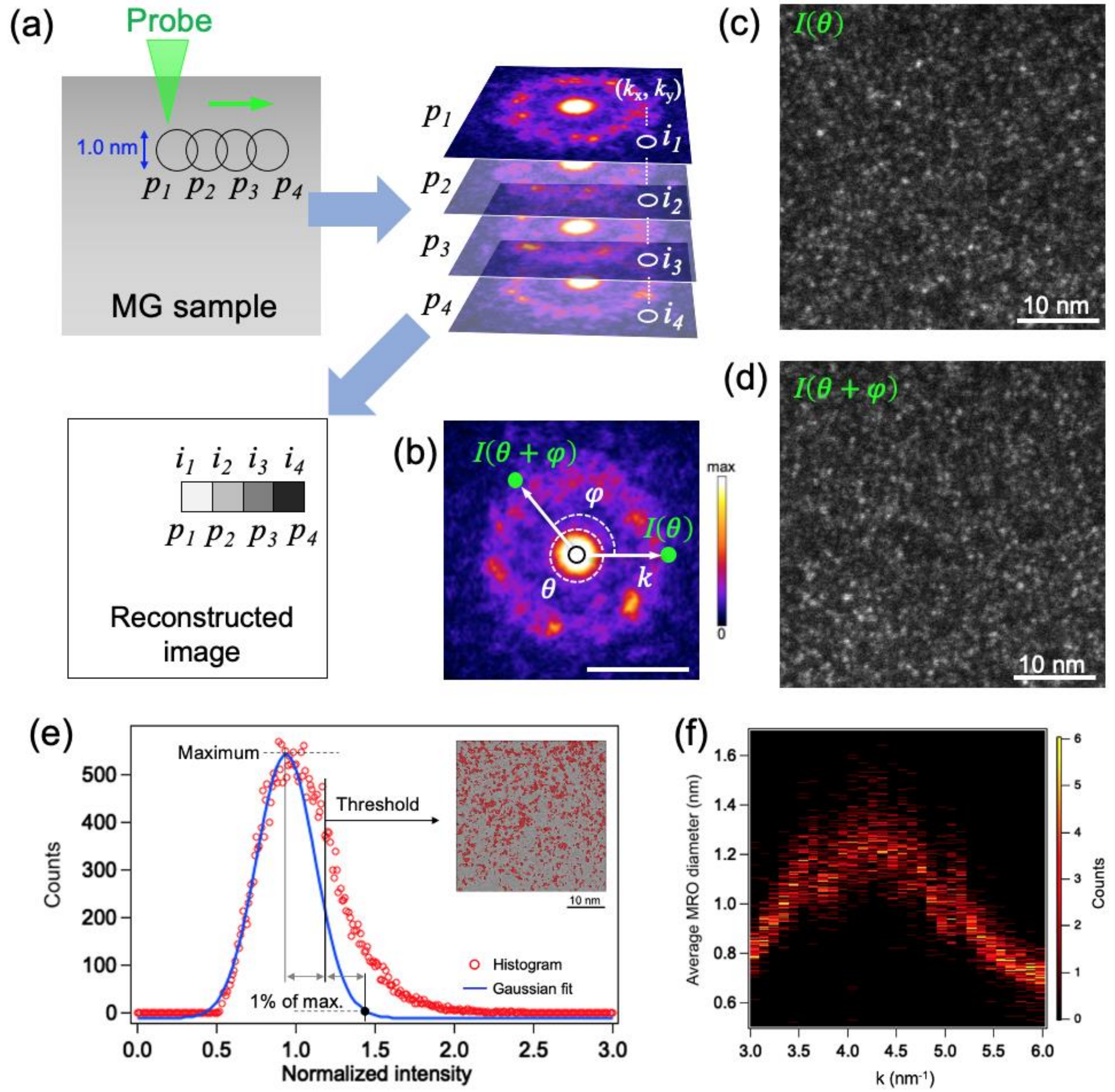

Figure 1. (a) Schematic of 4D-STEM. Nanodiffraction patterns are acquired using electron probe (diameter = 1 nm) from oversampled probe positions (p_1, p_2, ..) on the sample. The intensities (i_1, i_2 ,..) in the acquired stack of patterns are reconstructed in the real space by selecting any (k_x, k_y) pixel within the pattern. (b) An example nanodiffraction pattern. (c and d) The reconstructed dark-field images using the "$I(\theta)$" and "$I(\theta + \varphi)$" locations in (b), respectively. (e) An example histogram of the normalized pixel intensities within a reconstructed image (red circles), a Gaussian fit to the left side of the histogram (blue line), and the location of the threshold value. The inset shows a dark field image from $Zr_{45}Cu_{50}Al_5$ (x = 0) after the threshold mask is applied. Red areas indicate the areas with high intensity above the threshold. (f) 2-D histograms of the average MRO diameter (in nm) as a function of k, calculated from the dark field images.

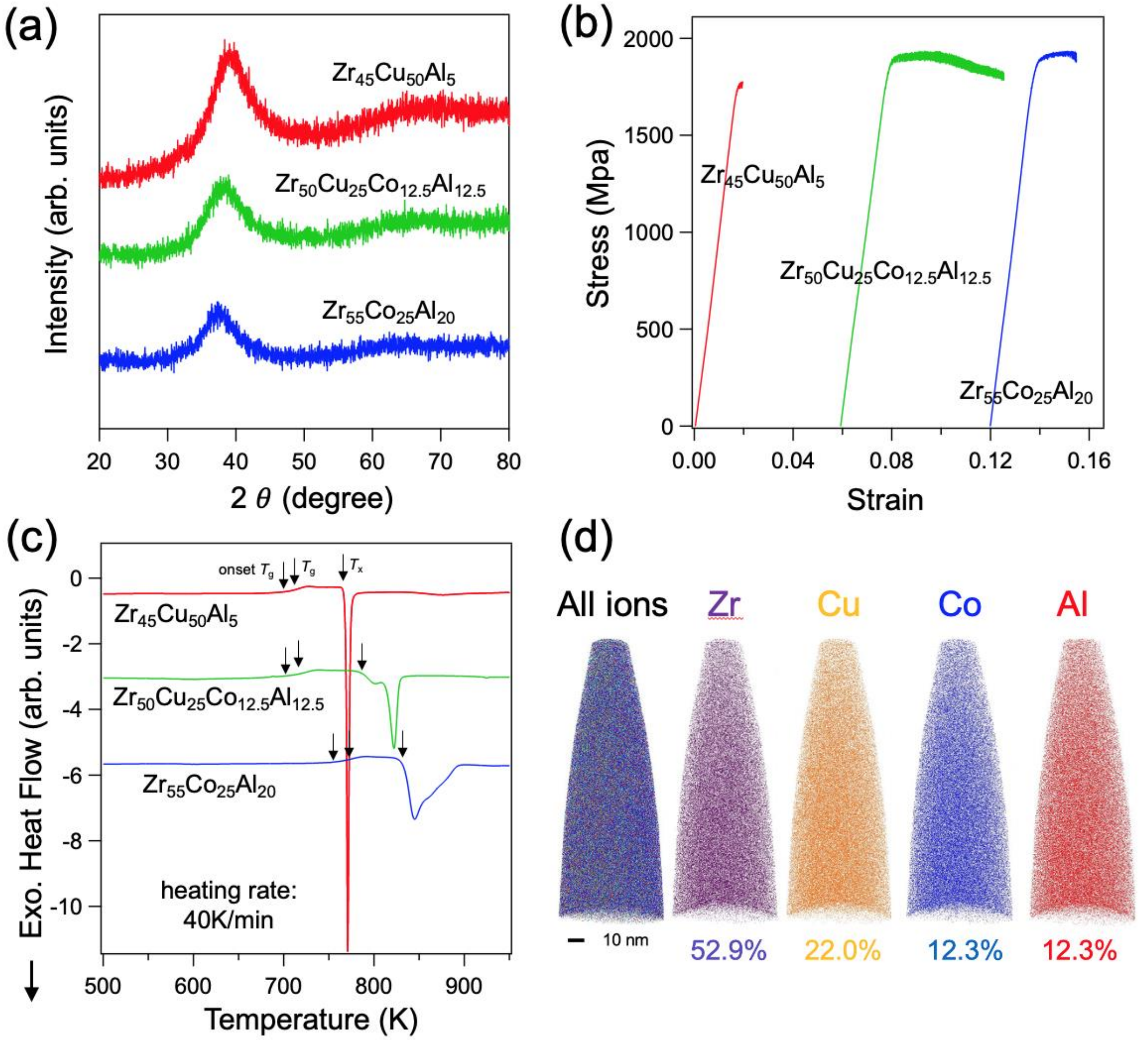

Figure 2. Experimental (a) X-ray diffraction, (b) compression, (c) DSC, and (d) atom probe tomography data from $(Zr_{45}Cu_{50}Al_5)_{1-x}(Zr_{55}Co_{25}Al_{20})_x$ (x = 0, 0.5, and 1).

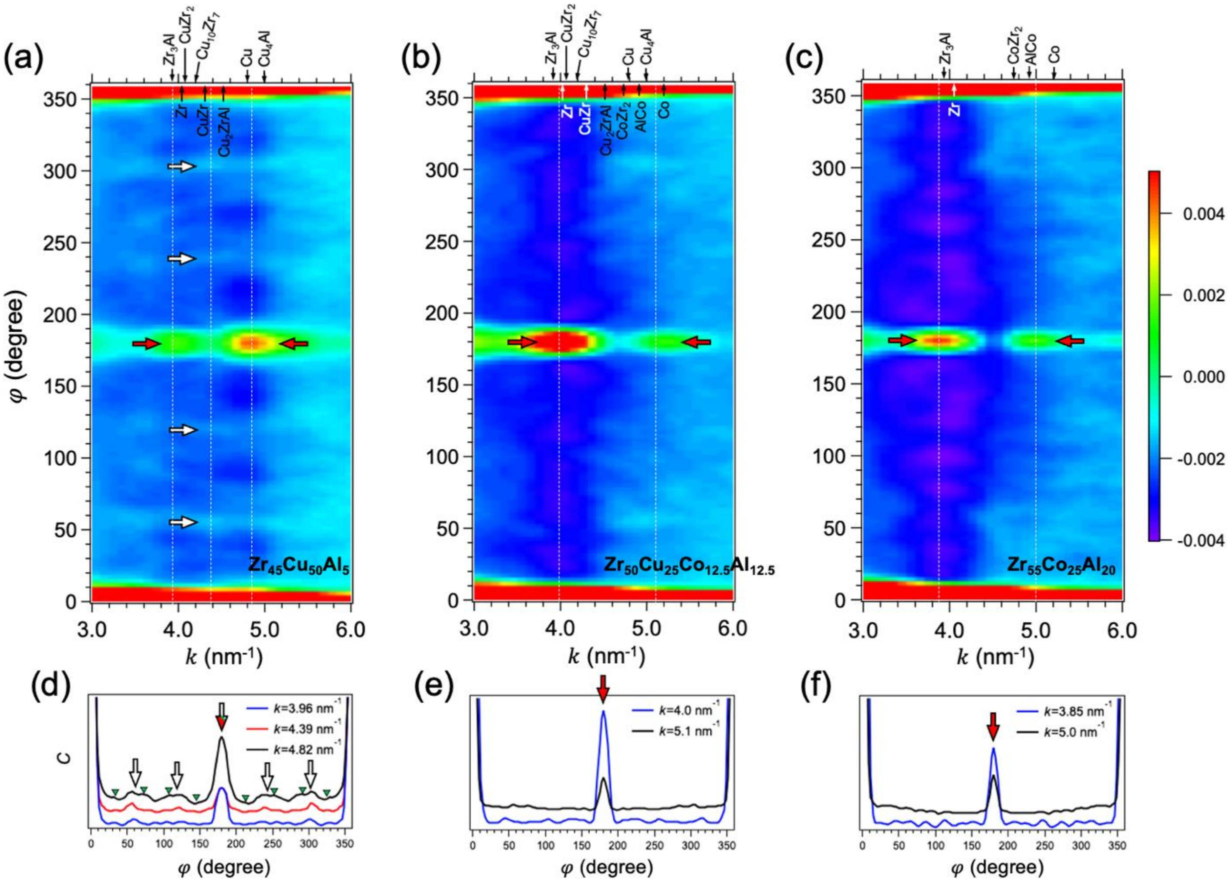

Figure 3. Maps of averaged angular correlation, $C(\varphi)$, as a function of k, from (a) $Zr_{45}Cu_{50}Al_5$ (x = 0), (b) $Zr_{50}Cu_{25}Co_{12.5}Al_{12.5}$ (x = 0.5), and (c) $Zr_{55}Co_{25}Al_{20}$ (x = 1). (d, e, and f) The line profiles for different k values indicated with the white dashed lines on (a), (b), and (c), respectively. In (d), the profiles are shifted vertically for visual clarity.

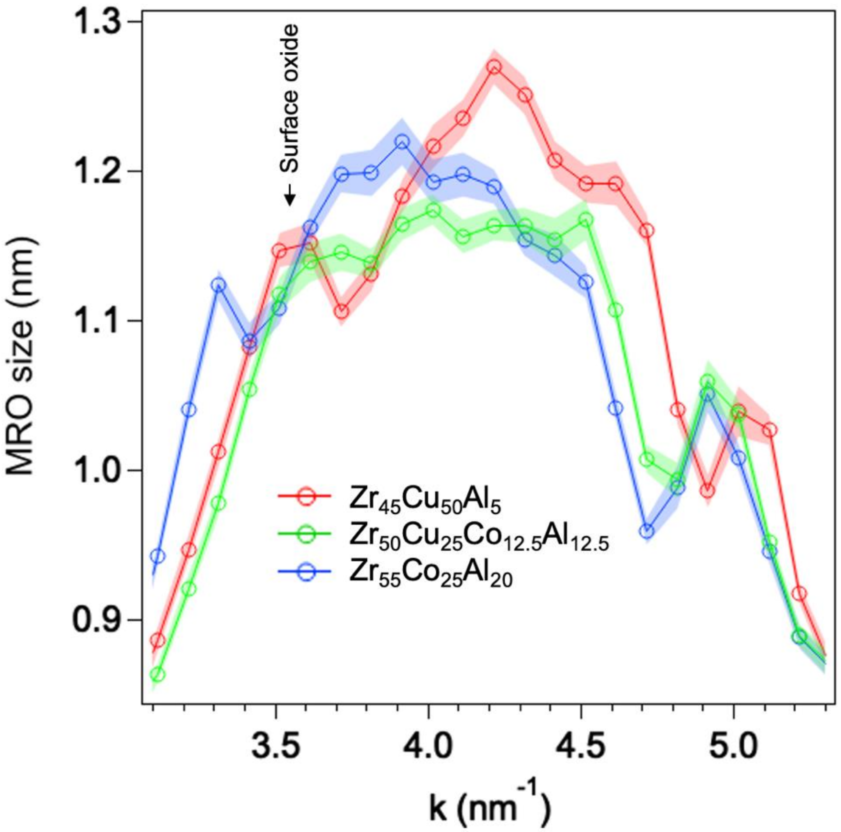

Figure 4. Average MRO size vs. *k* from $Zr_{45}Cu_{50}Al_5$ ($x = 0$), $Zr_{50}Cu_{25}Co_{12.5}Al_{12.5}$ ($x = 0.5$), and $Zr_{55}Co_{25}Al_{20}$ ($x = 1$). Color shadows indicate standard deviation of mean.

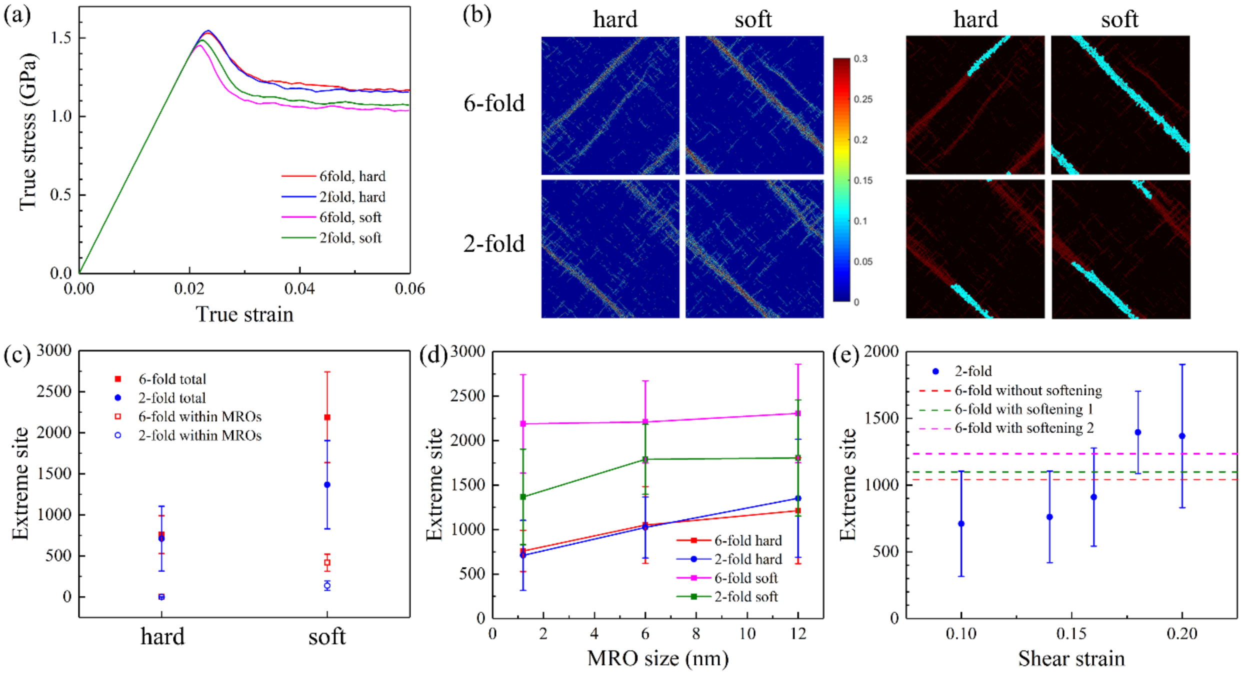

Figure 5. (a) Simulated stress-strain curves for $(Zr_{45}Cu_{50}Al_5)_{1-x}(Zr_{55}Co_{25}Al_{20})_x$ (6-fold for $x = 0$ and 2-fold for $x = 0.5$) with hard and soft MROs. (b) The deformation microstructures (Von Mises strain maps) at 2.7% overall elongation for all four curves in (a) at left two columns, and the Von Mises strain maps (red dots) at 3% overall elongation and superposition of the largest connected-free-volume (cyan dots) on top of them. (c) Average numbers of extreme sites of the whole system and within the MROs, together with the error representing the standard deviation. (d) Average numbers of extreme sites with different MRO sizes, with the error being the standard deviation. (e) Average numbers of extreme sites with different shear strain for 2-fold MRO regions without softening, and the average numbers of extreme sites for 6-fold MRO regions with different softening behaviors as references (dash lines).